PAPER

Check for updates

Crystal growth control of rod-shaped ε-Fe₂O₃ nanocrystals†

Hiroko Tokoro, [ID] *[ab] Junpei Fukui,[a] Koki Watanabe,[a] Marie Yoshikiyo, [ID] [b] Asuka Namai[b] and Shin-ichi Ohkoshi [ID] *[b]

Herein we report crystal growth control of rod-shaped ε-Fe₂O₃ nanocrystals by developing a synthesis based on the sol–gel technique using β-FeO(OH) as a seed in the presence of a barium cation. ε-Fe₂O₃ nanocrystals are obtained over a wide calcination temperature range between 800 °C and 1000 °C. A low calcination temperature (800 °C) provides an almost cubic rectangular-shaped ε-Fe₂O₃ nanocrystal with an aspect ratio of 1.4, whereas a high calcination temperature (1000 °C) provides an elongated rod-shaped ε-Fe₂O₃ nanocrystal with an aspect ratio of 3.3. Such systematic anisotropic growth of ε-Fe₂O₃ is achieved due to the wide calcination temperature in the presence of barium cations. The surface energy and the anisotropic adsorption of barium on the surface of ε-Fe₂O₃ can explain the anisotropic crystal growth of rod-shaped ε-Fe₂O₃ along the crystallographic *a*-axis. The present work may provide important knowledge about how to control the anisotropic crystal shape of nanomaterials.

Introduction

Ferrite magnets are ubiquitous functional materials for industry due to their ferromagnetic properties.[1–6] Among ferrite magnets, gamma-diiron trioxide (γ-Fe₂O₃) has been extensively used due to its soft magnetic functionalities and chemical stability.[7–10] On the other hand, epsilon-diiron trioxide (ε-Fe₂O₃) has drawn increasing attention in recent years.[11–16] In 2004, a single phase of ε-Fe₂O₃, which was artificially synthesized *via* a nanoscale synthesis, displayed a huge magnetic coercive field over 20 kOe at room temperature.[11] Since then, various fundamental studies have been reported.[17–23] Furthermore, practical applications such as high-density magnetic recordings and high-frequency electromagnetic (EM) wave absorption have been considered.[24–27] From a synthetic viewpoint, different methods for ε-Fe₂O₃ have been reported, including the reverse-micelle and sol–gel combination, mesoporous SiO₂ template, pulsed laser deposition (PLD), and chemical vapor deposition (CVD).[17,28–34]

The ε-Fe₂O₃ phase is only formed in the nanosize region. Typically, ε-Fe₂O₃ nanoparticles have a spherical shape, but rod-shaped crystals can appear under specific conditions.[12]

Rod-shaped ε-Fe₂O₃ has received attention from the viewpoint of applications as oriented fibers and probes for magnetic force microscopy.[12,35] For example, small rod-shaped ε-Fe₂O₃ crystals less than a hundred nanometers are attractive for an oriented optical material because light scattering is eliminated. By contrast, elongated rod-shaped ε-Fe₂O₃ crystals are desirable as a probe in magnetic force microscopy. Hence, controlling the particle size of rod-shaped ε-Fe₂O₃ nanocrystals is an important issue. To date, rod-shaped ε-Fe₂O₃ nanocrystals have only been obtained using a combination of reverse-micelle and sol–gel techniques.[12] However, this method produces ε-Fe₂O₃ in a very limited calcination temperature region (*i.e.*, 960–1040 °C), highlighting the difficulty in controlling the particle size. A method to control the particle size of rod-shaped ε-Fe₂O₃ has yet to be developed. In this work, we report a synthetic method to prepare rod-shaped ε-Fe₂O₃ nanocrystals with a wide range of calcination temperatures to control the particle size and investigate a long-standing problem: the mechanism of anisotropic crystal growth of rod-shaped ε-Fe₂O₃.

Here, we report the synthesis of rod-shaped ε-Fe₂O₃ nanocrystals based on the sol–gel technique using β-FeO(OH) as a seed with a SiO₂ matrix. X-ray powder diffraction (XRPD) and Rietveld analyses indicate that ε-Fe₂O₃ can be obtained by calcination over a wide temperature range (*i.e.*, 800–1000 °C). Transmission Electron Microscopy (TEM) shows that the size of the rod-shaped crystals is well controlled over a wide range of calcination temperatures. The anisotropic crystal growth of rod-shaped ε-Fe₂O₃ can be explained using the surface energy and anisotropic adsorption of barium on the crystal surface.

aDepartment of Materials Science, Faculty of Pure and Applied Sciences, University of Tsukuba, 1-1-1 Tennodai, Tsukuba, Ibaraki 305-8573, Japan. E-mail: tokoro@ims.tsukuba.ac.jp

bDepartment of Chemistry, School of Science, The University of Tokyo, 7-3-1 Hongo, Bunkyo-ku, Tokyo 113-0033, Japan. E-mail: ohkoshi@chem.s.u-tokyo.ac.jp

† Electronic supplementary information (ESI) available: Results of crystal structural analyses, particle sizes obtained by TEM images, magnetic hysteresis loops, crystal shape and crystallographic direction of ε-Fe₂O₃ crystal, and surface energy in ε-Fe₂O₃. See DOI: 10.1039/d0ra07256g

Materials and methods

Materials

Fig. 1 schematically illustrates the synthesis of rod-shaped ε-Fe_2O_3 nanocrystals based on the sol–gel technique using β-FeO(OH) as a seed with a SiO_2 matrix. Barium nitrate ($Ba(NO_3)_2$) (0.5 g) was added to water-dispersible β-FeO(OH) (4 g) solution (420 mL) (Taki Chemical; Fe–C10). An aqueous solution of 25% ammonia (19.2 mL) was added to a β-FeO(OH) dispersed solution. The mixture was stirred at 50 °C for 30 min. Then tetraethoxysilane (TEOS, $Si(C_2H_5O)_4$) (24 mL) was added, and the solution was stirred at 50 °C for 20 h. The resultant orange gel was collected by centrifugation, washed with water, and dried at 60 °C for 1 day. The obtained orange powder was calcinated at 800–1000 °C for 4 h in air. The calcinated powder was etched with a NaOH aqueous solution at 70 °C to remove the SiO_2 matrix that covered the iron oxide nanocrystals. The etched powder was washed with hydrochloric acid. In this work, we prepared 7 samples calcinated at different temperatures: 800 °C (**1**), 850 °C (**2**), 875 °C (**3**), 900 °C (**4**), 950 °C (**5**), 975 °C (**6**), and 1000 °C (**7**).

Physical measurements

XRPD patterns were measured by a Rigaku Ultima IV using Cu Kα ($\lambda = 1.5418$ Å). Rietveld analyses for the XRPD patterns were performed using Rigaku PDXL software. TEM images were acquired using a JEOL JEM 2000EX. TEM energy-dispersive X-ray spectroscopy (TEM-EDX) was performed using a JEOL JEM

2010F. Raman spectra were measured by NRS-5500 Laser Raman Spectrometer (JASCO Corporation, Japan). Magnetic measurements were performed using a Quantum Design MPMS superconducting quantum interference device (SQUID) magnetometer.

Results and discussion

Crystal structure, morphology, and magnetic properties of the nanocrystals

Fig. 2 shows the XRPD patterns with Rietveld analyses of the obtained samples. Sample **1** contains 97.2% of ε-Fe_2O_3 with an orthorhombic crystal structure in the $Pna2_1$ space group and lattice constants of $a = 5.064(8)$ Å, $b = 8.729(14)$ Å, and $c = 9.610(9)$ Å (Fig. 2b and S1, Table S1†). In addition, a slight amount of γ-Fe_2O_3 with a cubic crystal structure in the $Fd\bar{3}m$

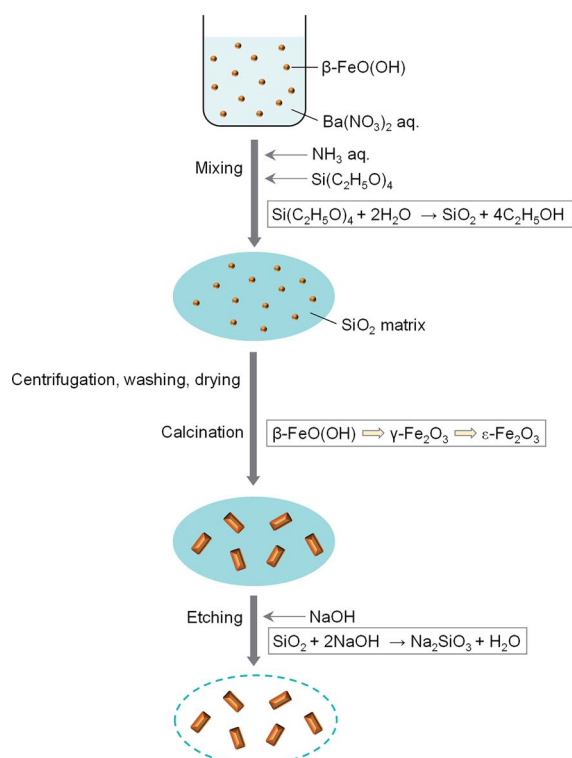

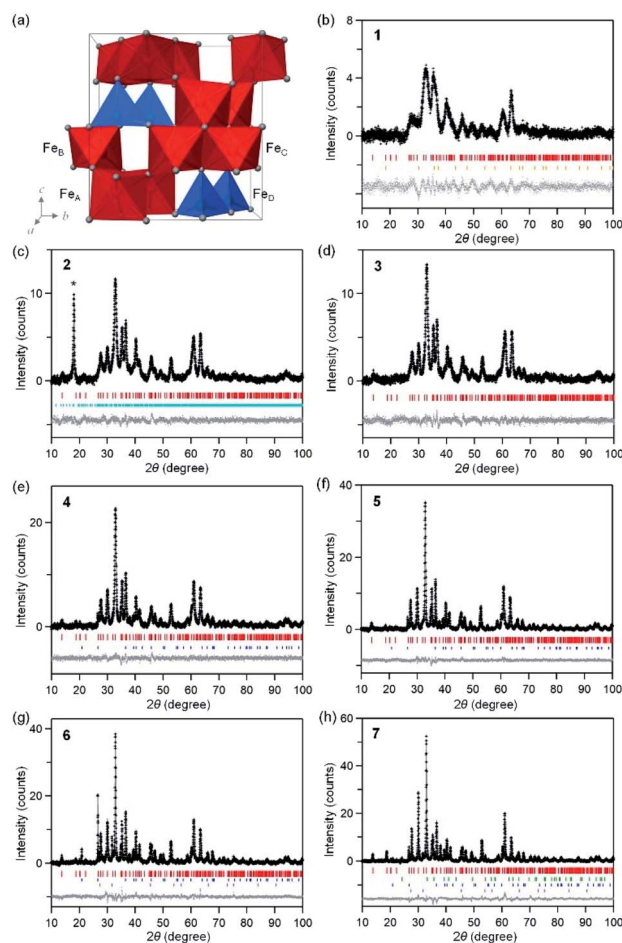Fig. 1 Schematic of the synthesis for rod-shaped ε-Fe_2O_3 nanocrystals.

Fig. 2 (a) Crystal structure of the orthorhombic unit cell of ε-Fe_2O_3. Red and blue polyhedrals in the crystal structure indicate octahedral and tetrahedral Fe sites, respectively. Gray balls represent oxygen atoms. XRPD patterns and Rietveld analyses for **1** (b), **2** (c), **3** (d), **4** (e), **5** (f), **6** (g), and **7** (h). Black dots, gray lines, and gray dots are the observed patterns, calculated patterns, and their differences, respectively. Colored bars indicate the calculated Bragg reflection positions for ε-Fe_2O_3 (red), γ-Fe_2O_3 (orange), α-Fe_2O_3 (green), and a slight amount of impurities of $Na_2Si_4O_8$ (light blue), SiO_2 (blue), and NaCl (purple). Asterisk in (c) indicates the peak of $Na_2Si_2O_8$.

space group and a lattice constant of $a = 8.299(4)$ Å) is present. Samples **2–6** consist of ε-Fe$_2$O$_3$ as a single phase of iron oxide (Fig. 2c–g). In sample **7**, ε-Fe$_2$O$_3$ is the dominant phase but a slight amount of α-Fe$_2$O$_3$ with a hexagonal crystal structure in the $R\bar{3}c$ space group and lattice constants of $a = 5.0353(9)$ Å and $c = 13.752(3)$ Å is generated as a nominal phase (Fig. 2h). Fig. S2† shows the phase fraction *versus* temperature in a phase diagram for iron oxide. A single-phase of ε-Fe$_2$O$_3$ is obtained in a wide calcination temperature range. In the low calcination temperature region, a slight amount of γ-Fe$_2$O$_3$ appears. On the other hand, α-Fe$_2$O$_3$ is generated as a nominal phase in the high calcination temperature region. This phase diagram is consistent with the previous study, which reported that ε-Fe$_2$O$_3$ is generated as a stable intermediate phase between γ-Fe$_2$O$_3$ and α-Fe$_2$O$_3$.[29]

Fig. 3 and Table S2† show the TEM images of the samples and the obtained particle size distributions. In sample **1**, the nanoparticles have an almost cubic shape with average sizes of 11.9 ± 3.5 nm for the long axis and 8.4 ± 1.9 nm for the short axis. The particle size distribution follows a log-normal distribution (Fig. S3†). The aspect ratio (the long axis to the short axis) of **1** is 1.4. In sample **2**, the average sizes of the long and short axes are 22.2 ± 8.1 nm and 12.5 ± 3.2 nm, respectively. The aspect ratio is 1.8. As the calcination temperature increases, in samples **3–7**, the size of the long axis abruptly increases while the size of the short axis gradually increases (*i.e.*, the aspect ratio increases as shown in Fig. 3h). In sample **7**, the nanoparticle has an elongated shape, and the average sizes of the long and short axes are 93.2 ± 105 nm and 28.2 ± 12.2 nm, respectively. This gives an aspect ratio of 3.3. As the calcination temperature increases, the long axis grows, leading to an elongated rod-shape. In the case of the reported spherical-shaped particles, changing the calcination temperature controls the size. For example, the diameter is 5.5 ± 1.6 nm at 902 °C, 5.6 ± 1.6 nm at 951 °C, and 7.8 ± 2.7 nm at 1002 °C.[32] The particle sizes are considerably smaller than the rod-shaped ε-Fe$_2$O$_3$ synthesized by the present method. This difference indicates that barium promotes crystal growth of ε-Fe$_2$O$_3$.

Fig. S4† shows the magnetic hysteresis loops at room temperature up to 7 Tesla. The magnetic coercive field (H_c) value increases as the calcination temperature increases (*i.e.*, the particle size increases). This observed trend corresponds to the reported trend where H_c increases as the particle size increases because the superparamagnetic effect operates in a small particle region.[32,36,37] The magnetization values for **1–5** become higher as the calcination temperature increases. However, in **6** and **7**, the magnetization values are low, even though the calcination temperature is high. One possible reason for the low magnetization is the formation of a slight amount of α-Fe$_2$O$_3$ (Fig. S5†), which is not observed in the XRD measurement.[38] Another reason, it is speculated that when the particle shape becomes elongated into a rod, the particles are likely to overlap with each other due to the magnetic force. The rod-shaped ε-Fe$_2$O$_3$ particle is confirmed to be a single domain magnet.[35] In such a case, the magnetic moments of ε-Fe$_2$O$_3$ particles may cancel each other. Consequently, the net total magnetization becomes smaller.
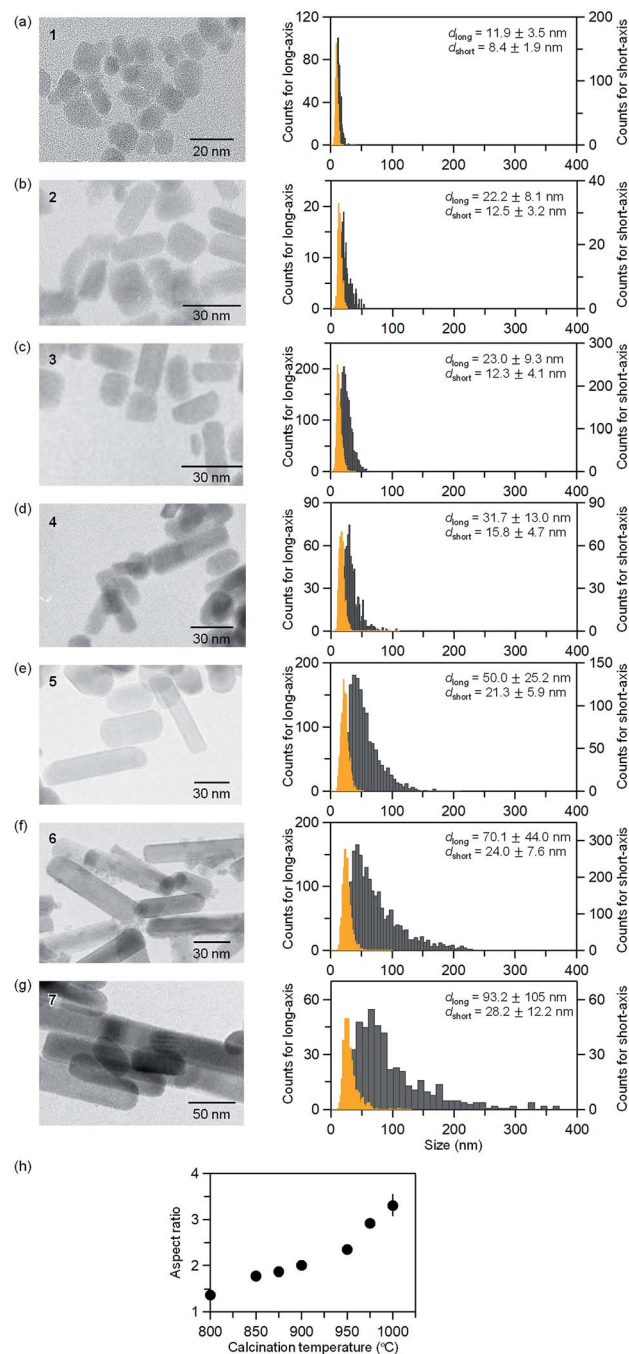

Fig. 3 TEM images for samples (a) **1**, (b) **2**, (c) **3**, (d) **4**, (e) **5**, (f) **6**, and (g) **7** (left). Particle size distributions of the long-axis (d_{long}) (gray) and the short-axis (d_{short}) (orange) for **1–7** (right). (h) Calcination temperature dependence of the aspect ratio estimated from the average size obtained by the TEM images.

The mechanism of anisotropic crystal growth

Next, the origin of high anisotropic crystal growth of rod-shaped ε-Fe$_2$O$_3$ is examined. The TEM images show that the ε-Fe$_2$O$_3$ particle is a single crystal and the longitudinal direction of rod-shaped ε-Fe$_2$O$_3$ is the crystallographic *a*-axis (*i.e.*, the [100] direction) (Fig. 4a).[39] Hence, rod-shaped ε-Fe$_2$O$_3$ nanocrystal is
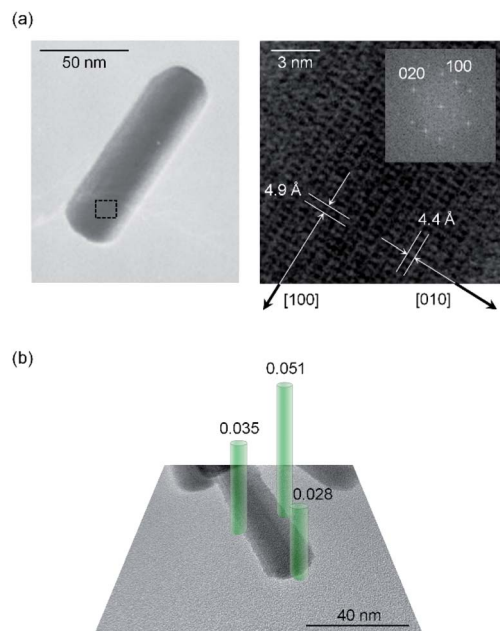
Fig. 4 (a) TEM image of **7**. Rod-shaped ε-Fe_2O_3 shows that the longitudinal direction is along the crystallographic a-axis of ε-Fe_2O_3 ([100] direction). Right figure is an enlarged view of the dotted-line frame in the left figure. Inset shows the Fourier transformed image. (b) TEM image of **6** showing the Ba concentrations of different areas on the rod-shaped ε-Fe_2O_3 (green bars). Ba concentrations are measured by EDX and calculated as the molar ratio with respect to the Fe_2O_3 formula. Green bar diameters indicate the spot sizes of the EDX measurement.

Fig. 5 Schematic of the lattice planes (green plane), values of surface energy (α_{hkl}, nm^{-2}), and number of FeO_6-broken bond per area (N_{hkl}, nm^{-2}) for the rod-shaped ε-Fe_2O_3 nanocrystals (Table S3†). Red, blue, and gray spheres in the crystal structure indicate the Fe at octahedral site, Fe at tetrahedral site, and O, respectively. Large α and small N values indicate the easy-growth plane.

a rectangular-type rod with the long axis in the [100] direction (Fig. S6†).

To understand the anisotropic crystal growth of the nano-rod along the [100] direction, we calculated the surface energies of the (hkl) planes, α_{hkl}, based on the binding energy of each surface. α_{hkl} is expressed by $\alpha_{hkl} = \Sigma E_{hkl}/S_{hkl}$, where ΣE_{hkl} is the sum of the binding energies of the broken bonds at the (hkl) plane and S_{hkl} is the area of the lattice plane.[40] Assuming equal binding energies between all Fe and O sites, the magnitude of the surface energies for typical lattice planes are calculated as: 19.2 nm^{-2} (100), 18.7 nm^{-2} (010), 13.4 nm^{-2} (001), 19.0 nm^{-2} (110), 11.9 nm^{-2} (011), 19.7 nm^{-2} (101), and 17.8 nm^{-2} (111) (Table S3†). The (100), (101), and (111) planes possess high surface energies (Fig. 5), whereas the (001) and (011) planes show low surface energies (Fig. S7†). Hence, the (100), (101), and (111) planes are candidates for the growth crystallographic planes.

Next, we focused on the barium adsorption effect. Fig. 4b shows the results of EDX measurement in TEM to investigate the distribution of the barium around the particles. The green cylinders indicate the areas of the EDX measurements. The calculated molar ratios of barium for each area with respect to the Fe_2O_3 formula indicate larger values at the longitudinal side of the rods compared to the edge of the short axis. These results suggest that a larger amount of barium is adsorbed on the longitudinal side of the rod than on the edge surface of the
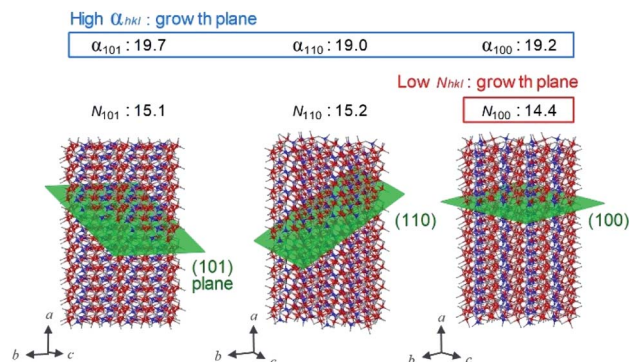
growth direction. We considered the mechanism of anisotropic crystal growth of ε-Fe_2O_3 from the viewpoint of anisotropic adsorption of barium on the surface of ε-Fe_2O_3 particles. In the calcination process, melting SiO_2 matrix (Si^{4+} and O^{2-}) and Ba^+ ion exist around ε-Fe_2O_3 particles. Since Ba^+ ion takes an octahedral BaO_6 coordination geometry with oxygen,[41,42] barium should be adsorbed on the surface of ε-Fe_2O_3 in the form of pseudo-octahedral BaO_6. On the other hand, on the surface of ε-Fe_2O_3 particles, there are two kinds of broken bonds (*i.e.*, broken octahedral FeO_6 and broken tetrahedral FeO_4). Since BaO_6 should be adsorbed at the octahedral FeO_6 site rather than at the tetrahedral FeO_4 site, a surface containing a large amount of FeO_6-broken bonds should be covered with adsorbed barium, suppressing crystal growth (*i.e.*, the growth surface should be the one with a small amount of FeO_6-broken bonds). We estimated the number of FeO_6-broken bonds per area, N_{hkl}. Fig. 5 and Table S3† show that the N_{hkl} values are 14.4 nm^{-2}, 15.2 nm^{-2}, and 15.1 nm^{-2} for (100), (110), and (101) planes, respectively. N_{100} shows the lowest value. These values indicate that the [100] direction, along the a-axis, can be the crystal growth direction because barium is less adsorbed on the surface of the (100) plane compared to other planes.

Conclusions

Rod-shaped ε-Fe_2O_3 nanocrystals are synthesized based on the sol–gel technique using β-FeO(OH) as a seed in the presence of a barium cation. In this method, changing the calcination temperature can control the size of rod-shaped ε-Fe_2O_3 nanocrystals. A low calcination temperature provides almost cubic rectangular-shaped ε-Fe_2O_3 nanocrystals, whereas a high calcination temperature provides elongated rod-shaped ε-Fe_2O_3 nanocrystals. Although the mechanism of anisotropic crystal growth of rod-shaped ε-Fe_2O_3 has been a long-standing issue, in this work, the surface energy and the anisotropic adsorption of barium on the surface of ε-Fe_2O_3 can explain the anisotropic crystal growth of the rod-shaped ε-Fe_2O_3 along the

crystallographic *a*-axis. These findings should realize hard magnetic ferrite ε-Fe$_2$O$_3$ nanocrystals for practical applications and provide important knowledge about how to control the anisotropic crystal shape of the nanomaterials.

Conflicts of interest

The authors declare no competing financial interest.

Acknowledgements

Notes and references

1 D. J. Craik, *Magnetic oxides*, Wiley, London, 1975.

2 *The Physics of Ul-tra-High Density Magnetic Recording*, ed. M. L. Plumer, J. van Ek, and D. Weller, Springer-Verlag, BerlinHei-delberg, 2001.

3 A. Goldman, *Modern Ferrite Technology*, 2nd edn, Springer, New York, 2006.

4 C. T. Yavuz, J. T. Mayo, W. W. Yu, A. Prakash, J. C. Falkner, S. Yean, L. Cong, H. J. Shipley, A. Kan, M. Tomson, D. Natelson and V. L. Colvin, Low-Field Magnetic Separation of Monodisperse Fe$_3$O$_4$ Nanocrystals, *Science*, 2006, **314**, 964–967.

5 Y. Nakamura, *Advanced Technologies of Perpendicular Magnetic Recording*, CMC Publishing, Tokyo, 2007.

6 S. Laurent, D. Forge, M. Port, A. Roch, C. Robic, L. V. Elst and R. N. Muller, Magnetic Iron Oxide Nanoparticles: Synthesis, Stabilization, Vectorization, Physicochemical Characterizations, and Biological Applications, *Chem. Rev.*, 2008, **108**, 2064–2110.

7 G. A. Challis, Pyrite–haematite alteration as a source of colour in red beds and regolith, *Nature*, 1975, **255**, 471–472.

8 R. F. Ziolo, E. P. Giannelis, B. A. Weinstein, M. P. O'Horo, B. N. Ganguly, V. Mehrotra, M. W. Russell and D. R. Huffman, Matrix-mediated synthesis of nanocrystalline γ-Fe$_2$O$_3$: a new optically transparent magnetic material, *Science*, 1992, **257**, 219–223.

9 E. T. Lacheisserie, D. Gignoux and M. Schlenker, *Magnetism: II-Materials & Applications*, Kluwer, Norwell, 2002.

10 F. X. Redl, K.-S. Cho, C. B. Murray and S. O'Brien, Three-dimensional binary superlattices of magnetic nanocrystals and semiconductor quantum dots, *Nature*, 2003, **423**, 968–971.

11 J. Jin, S. Ohkoshi and K. Hashimoto, Giant Coercive Field of Nanometer-Sized Iron Oxide, *Adv. Mater.*, 2004, **16**, 48–51.

12 S. Ohkoshi and H. Tokoro, Hard Magnetic Ferrite: ε-Fe$_2$O$_3$, *Bull. Chem. Soc. Jpn.*, 2013, **86**, 897–907.

13 E. Tronc, C. Chanéac and J. P. Jolivet, Structural and magnetic characterization of ε-Fe$_2$O$_3$, *J. Solid State Chem.*, 1998, **139**, 93–104.

14 M. Kurmoo, J. L. Rehspringer, A. Hutlova, C. D'Orléans, S. Vilminot, C. Estournès and D. Niznansky, Formation of Nanoparticles of ε-Fe$_2$O$_3$ from Yttrium Iron Garnet in a Silica Matrix: An Unusually Hard Magnet with a Morin-Like Transition below 150 K, *Chem. Mater.*, 2005, **17**, 1106–1114.

15 Y. Kusano, T. Fujii, J. Takada, M. Fukuhara, A. Doi, Y. Ikeda and M. Takano, Epitaxial Growth of ε-Fe$_2$O$_3$ on Mullite Found through Studies on a Traditional Japanese Stoneware, *Chem. Mater.*, 2008, **20**, 151–156.

16 E. Taboada, M. Gich and A. Roig, Nanospheres of Silica with an ε-Fe$_2$O$_3$ Single Crystal Nucleus, *ACS Nano*, 2009, **3**, 3377–3382.

17 J. Jin, K. Hashimoto and S. Ohkoshi, Formation of spherical and rod-shaped ε-Fe$_2$O$_3$ nanocrystals with a large coercive field, *J. Mater. Chem.*, 2005, **15**, 1067–1071.

18 E. Tronc, C. Chaneac, J. P. Jolivet and J. M. Greneche, Spin collinearity and thermal disorder in ε-Fe$_2$O$_3$, *J. Appl. Phys.*, 2005, **98**, 053901.

19 M. Gich, C. Frontera, A. Roig, E. Taboada and E. Molins, High- and Low-Temperature Crystal and Magnetic Structures of ε-Fe$_2$O$_3$ and Their Correlation to Its Magnetic Properties, *Chem. Mater.*, 2006, **18**, 3889–3897.

20 S. Sakurai, K. Tomita, K. Hashimoto, H. Yashiro and S. Ohkoshi, Preparation of the Nanowire Form of ε-Fe$_2$O$_3$ Single Crystal and a Study of the Formation Process, *J. Phys. Chem. C*, 2008, **112**, 20212–20216.

21 Y.-C. Tseng, N. M. Souza-Neto, D. Haskel, M. Gich, C. Frontera, A. Roig, M. Veenendaal and J. Nogués, Nonzero orbital moment in high coercivity ε-Fe$_2$O$_3$ and low-temperature collapse of the magnetocrystalline anisotropy, *Phys. Rev. B: Condens. Matter Mater. Phys.*, 2009, **79**, 094404.

22 A. Namai, S. Sakurai, M. Nakajima, T. Suemoto, K. Matsumoto, M. Goto, S. Sasaki and S. Ohkoshi, Synthesis of an Electromagnetic Wave Absorber for High-Speed Wireless Communication, *J. Am. Chem. Soc.*, 2009, **131**, 1170–1173.

23 J. Tuček, S. Ohkoshi and R. Zbořil, Room-temperature ground magnetic state of ε-Fe$_2$O$_3$: in-field Mössbauer spectroscopy evidence for collinear ferrimagnet, *Appl. Phys. Lett.*, 2011, **99**, 253108.

24 S. Ohkoshi, S. Kuroki, S. Sakurai, K. Matsumoto, K. Sato and S. Sasaki, Inside Cover: a Millimeter-Wave Absorber Based on Gallium-Substituted ε-Iron Oxide Nanomagnets, *Angew. Chem., Int. Ed.*, 2007, **46**, 8392–8395.

25 J. Tuček, R. Zbořil, A. Namai and S. Ohkoshi, ε-Fe$_2$O$_3$: an Advanced Nanomaterial Exhibiting Giant Coercive Field, Millimeter-Wave Ferromagnetic Resonance, and Magnetoelectric Coupling, *Chem. Mater.*, 2010, **22**, 6483–6505.

26 A. Namai, M. Yoshikiyo, K. Yamada, S. Sakurai, T. Goto, T. Yoshida, T. Miyazaki, M. Nakajima, T. Suemoto, H. Tokoro and S. Ohkoshi, Hard magnetic ferrite with a gigantic coercivity and high frequency millimetre wave rotation, *Nat. Commun.*, 2012, **3**, 1035.

27 S. Ohkoshi, A. Namai, M. Yoshikiyo, K. Imoto, K. Tamasaki, K. Matsuno, O. Inoue, T. Ide, K. Masada, M. Goto, T. Goto, T. Yoshida and T. Miyazaki, Multimetal-Substituted Epsilon-Iron Oxide ε-$Ga_{0.31}Ti_{0.05}Co_{0.05}Fe_{1.59}O_3$ for Next-Generation Magnetic Recording Tape in the Big-Data Era, *Angew. Chem., Int. Ed.*, 2016, **55**, 11403–11406.

28 Y. Ding, J. R. Morber, R. L. Snyder and Z. L. Wang, Nanowire Structural Evolution from Fe_3O_4 to ε-Fe_2O_3, *Adv. Funct. Mater.*, 2007, **17**, 1172–1178.

29 S. Sakurai, A. Namai, K. Hashimoto and S. Ohkoshi, First Observation of Phase Transformation of All Four Fe_2O_3 Phases ($\gamma \rightarrow \varepsilon \rightarrow \beta \rightarrow \alpha$-Phase), *J. Am. Chem. Soc.*, 2009, **131**, 18299–18303.

30 G. Carraro, D. Barreca, C. Maccato, E. Bontempi, L. E. Depero, C. de J. Fernández and A. Caneschi, Supported ε and β iron oxide nanomaterials by chemical vapor deposition: structure, morphology and magnetic properties, *CrystEngComm*, 2013, **15**, 1039.

31 B. David, N. Pizúrová, P. Synek, V. Kudrle, O. Jašek and O. Schneeweiss, -Fe_2O_3 nanoparticles synthesized in atmospheric-pressure microwave torch, *Mater. Lett.*, 2014, **116**, 370–373.

32 S. Ohkoshi, A. Namai, K. Imoto, M. Yoshikiyo, W. Tarora, K. Nakagawa, M. Komine, Y. Miyamoto, T. Nasu, S. Oka and H. Tokoro, Nanometer-size hard magnetic ferrite exhibiting high optical-transparency and nonlinear optical-magnetoelectric effect, *Sci. Rep.*, 2015, **5**, 14414.

33 A. Sivkov, E. Naiden, A. Ivashutenko and I. Shanenkov, Plasma dynamic synthesis and obtaining ultrafine powders of iron oxides with high content of ε-Fe_2O_3, *J. Magn. Magn. Mater.*, 2016, **405**, 158–168.

34 H. Tokoro, W. Tarora, A. Namai, M. Yoshikiyo and S. Ohkoshi, Direct Observation of Chemical Conversion from Fe_3O_4 to ε-Fe_2O_3 by a Nanosize Wet Process, *Chem. Mater.*, 2018, **30**, 2888–2894.

35 S. Ohkoshi, A. Namai, T. Yamaoka, M. Yoshikiyo, K. Imoto, T. Nasu, S. Anan, Y. Umeta, K. Nakagawa and H. Tokoro, Mesoscopic bar magnet based on ε-Fe_2O_3 hard ferrite, *Sci. Rep.*, 2016, **6**, 27212.

36 In metal alloy systems, the coercive field increases as the rod-shaped particles become longer due to the dipole interaction between the particles.[37] In ε-Fe_2O_3, the magnitude of the coercive field does not change due to the particle shape. That is, spherical- and rod-shaped ε-Fe_2O_3 exhibit similar coercive fields ($\sim$20 kOe at room temperature).[32,35] Hence, the aforementioned dipole interaction is negligible. One possible reason that the dipole interaction is negligible may be the strong crystal magnetic anisotropy in ε-Fe_2O_3.

37 P. G. B. Gueye, J. L. Sánchez, E. Navarro, A. Serrano and P. Marín, Control of the Length of $Fe_{73.5}Si_{13.5}Nb_3Cu_1B_9$ Microwires to Be Used for Magnetic and Microwave Absorbing Purposes, *ACS Appl. Mater. Interfaces*, 2020, **12**, 15644–15656.

38 J. López-Sánchez, A. Serrano, A. del Campo, M. Abuín, E. Salas-Colera, A. Muñoz-Noval, G. R. Castro, J. de la Figuera, J. F. Marco, P. Marín, N. Carmona and O. Rodríguez de la Fuente, Self-assembly of iron oxide precursor micelles driven by magnetic stirring time in sol–gel coatings, *RSC Adv.*, 2019, **9**, 17571–17580.

39 The short-axis direction is diverse, *i.e.*, [010], [011], or [013] are observed as the short-axis directions.

40 J. Pelleg, L. Z. Zevin, S. Lungo and N. Croitoru, Reactive-sputter-deposited TiN films on glass substrates, *Thin Solid Films*, 1991, **197**, 117–128.

41 L. Liu, A Dense Modification of BaO and Its Crystal Structure, *J. Appl. Phys.*, 1971, **42**, 3702–3704.

42 R. B. Elo, S. P. Murarka and R. A. Swalin, A thermo-chemical study of the defect structure of barium oxide, *J. Phys. Chem. Solids*, 1973, **34**, 97–106.